



Martinović, Petra ; Barnewitz, Lars ; Rohdenburg, Markus ; Swiderek, Petra

Controlling electron beam induced deposition of iron from Fe(CO)₅: Inhibition of autocatalytic growth by NH₃ and reactivation by electron irradiation

Journal Article as: published version (Version of Record)

DOI of this document* (secondary publication): <https://doi.org/10.26092/elib/3706>

Publication date of this document: 19/02/2025

* for better findability or for reliable citation

Recommended Citation (primary publication/Version of Record) incl. DOI:

Petra Martinović, Lars Barnewitz, Markus Rohdenburg, Petra Swiderek; Controlling electron beam induced deposition of iron from Fe(CO)₅: Inhibition of autocatalytic growth by NH₃ and reactivation by electron irradiation. J. Vac. Sci. Technol. A 12 May 2023; 41 (3): 033207. <https://doi.org/10.1116/6.0002306>

Please note that the version of this document may differ from the final published version (Version of Record/primary publication) in terms of copy-editing, pagination, publication date and DOI. Please cite the version that you actually used. Before citing, you are also advised to check the publisher's website for any subsequent corrections or retractions (see also <https://retractionwatch.com/>).

This article may be downloaded for personal use only. Any other use requires prior permission of the author and AIP Publishing. This article appeared in Petra Martinović, Lars Barnewitz, Markus Rohdenburg, Petra Swiderek; Controlling electron beam induced deposition of iron from Fe(CO)₅: Inhibition of autocatalytic growth by NH₃ and reactivation by electron irradiation. J. Vac. Sci. Technol. A 12 May 2023; 41 (3): 033207 and may be found at <https://doi.org/10.1116/6.0002306>

This document is made available with all rights reserved.

Take down policy

If you believe that this document or any material on this site infringes copyright, please contact publizieren@suub.uni-bremen.de with full details and we will remove access to the material.

Controlling electron beam induced deposition of iron from $\text{Fe}(\text{CO})_5$: Inhibition of autocatalytic growth by NH_3 and reactivation by electron irradiation

Cite as: J. Vac. Sci. Technol. A 41, 033207 (2023); <https://doi.org/10.1116/6.0002306>

Submitted: 21 October 2022 • Accepted: 17 March 2023 • Published Online: 13 April 2023

 Petra Martinović,  Lars Barnewitz,  Markus Rohdenburg, et al.



ARTICLES YOU MAY BE INTERESTED IN

[On the limitations of thermal atomic layer deposition of InN using ammonia](#)

Journal of Vacuum Science & Technology A 41, 020401 (2023); <https://doi.org/10.1116/6.0002355>

[Conductive TiN thin films grown by plasma-enhanced atomic layer deposition: Effects of N-sources and thermal treatments](#)

Journal of Vacuum Science & Technology A 41, 032401 (2023); <https://doi.org/10.1116/6.0002288>

[Area selective atomic layer deposition of \$\text{SnO}_2\$ as an etch resist in fluorine based processes](#)

Journal of Vacuum Science & Technology A 41, 032402 (2023); <https://doi.org/10.1116/6.0002429>

HIDEN
ANALYTICAL

Instruments for Advanced Science

- Knowledge
- Experience ■ Expertise

[Click to view our product catalogue](#)

Contact Hiden Analytical for further details:

www.HidenAnalytical.com

info@hiden.co.uk

Gas Analysis

- ▶ dynamic measurement of reaction gas streams
- ▶ catalysis and thermal analysis
- ▶ molecular beam studies
- ▶ dissolved species probes
- ▶ fermentation, environmental and ecological studies

Surface Science

- ▶ UHVTPD
- ▶ SIMS
- ▶ end-point detection in ion beam etch
- ▶ elemental imaging - surface mapping

Plasma Diagnostics

- ▶ plasma source characterization
- ▶ etch and deposition process reaction kinetic studies
- ▶ analysis of neutral and radical species

Vacuum Analysis

- ▶ partial pressure measurement and control of process gases
- ▶ reactive sputter process control
- ▶ vacuum diagnostics
- ▶ vacuum coating process monitoring



Controlling electron beam induced deposition of iron from Fe(CO)₅: Inhibition of autocatalytic growth by NH₃ and reactivation by electron irradiation

Cite as: J. Vac. Sci. Technol. A 41, 033207 (2023); doi: 10.1116/6.0002306

Submitted: 21 October 2022 · Accepted: 17 March 2023 ·

Published Online: 13 April 2023



View Online



Export Citation



CrossMark

Petra Martinović,¹  Lars Barnewitz,¹  Markus Rohdenburg,²  and Petra Swiderek^{1,a)} 

AFFILIATIONS

¹Institute for Applied and Physical Chemistry (IAPC), Fachbereich 2 (Chemie/Biologie), University of Bremen, Leobener Str. 5 (NW2), Bremen 28359, Germany

²Wilhelm-Ostwald-Institute for Physical and Theoretical Chemistry (WOI), Leipzig University, Linnéstr. 2, Leipzig 04103, Germany

^{a)}Electronic-mail: swiderek@uni-bremen.de

ABSTRACT

Focused electron beam induced deposition (FEBID) is a versatile direct-write approach to produce nanostructures from organometallic precursor molecules. Ideally, the material is deposited only when precursors interact with and are dissociated by the impinging electrons so that the process is spatially defined by the electron beam. In reality, however, thermal surface reactions as known from chemical vapor deposition can also contribute to the dissociation of the precursors. They often produce material with higher purity but can also impair the spatial selectivity of the electron-induced deposit growth. This work aims at an approach to suppress such thermal chemistry and to re-enable it within an area defined by the electron beam. We have, thus, used a surface science approach to study the inhibition of autocatalytic growth (AG) of Fe from Fe(CO)₅ by NH₃ and the reactivation of AG on the surface by electron irradiation. The experiments were performed under ultrahigh vacuum conditions using thermal desorption spectrometry to characterize adsorption and reactivity of Fe(CO)₅ on Fe seed layers that were prepared by dosing Fe(CO)₅ during electron irradiation of the entire sample surface (referred to as EBID herein). Auger electron spectroscopy was used to monitor deposit growth and to reveal the potential inhibition of AG by NH₃ as well as the reactivation of the surface by electron irradiation. The results show that adsorption of NH₃ slows down AG on deposits prepared by EBID but not on Fe layers produced by AG. Electron irradiation after adsorption of NH₃ reactivates the surface and thus re-establishes AG. We propose that co-injection of NH₃ during FEBID from Fe(CO)₅ could be a viable strategy to suppress unwanted AG contributions and, therefore, enhance the spatial control of the deposition process.

Published under an exclusive license by the AVS. <https://doi.org/10.1116/6.0002306>

I. INTRODUCTION

Focused electron beam induced deposition (FEBID) is a flexible direct-write approach to the fabrication of nanoscale materials.^{1,2} In FEBID, the electrons that impinge on a surface initiate decomposition of adsorbed precursor molecules that contain the element of the desired material. The target element, typically a metal, is surrounded by ligands that provide the precursor with sufficient volatility to be dosed onto the surface via the gas phase. In an ideal case, the ligands are converted to volatile species upon fragmentation of the precursor, while the desired element would be

deposited on the underlying surface at the site where the electron-precursor interaction has occurred.

In reality, FEBID processes are more complex than this simple picture suggests. Typically, part of the ligand material is incorporated in the deposit, which leads to low metal contents¹⁻⁵ and calls for approaches to remove the unwanted elements.⁶⁻⁹ On top of this, the view that growth is determined exclusively by electron impact is also not correct. In fact, thermal surface reactions as known from chemical vapor deposition (CVD) processes can contribute to the formation of the non-volatile material.⁵ For instance,

freestanding nanoscale pillar-shaped deposits produced from the precursor Cu(hfac)(VTMS) were found to exhibit a low Cu content with high amount of remaining carbon at their base, while the material was turned into pure polycrystalline Cu at the top of the pillars when a certain length was reached.¹⁰ It was proposed that this effect relates to the low heat conductivity of thin pillar structures. This leads to the heating of the material at the top when targeted by the electron beam and, thus, to thermal decomposition of the precursor. This means that a transition from a pure FEBID process governed by the impinging electrons to a process with contributions of CVD can occur during the growth of the deposit. Such a transition was also observed between the center and the halo region of a dot deposit produced from the novel Ag precursor Ag(I) 2,2-dimethylbutanoate.¹¹ In the halo region, where the electron density is lower, the Ag content was significantly higher, and larger crystallites were formed. This again points to contributions of thermal CVD-type growth to the deposition process, likely initiated by small metallic seed particles formed by electron impact. As a third example, a similar change in growth mode has also been reported for thin pillars grown from iron pentacarbonyl, Fe(CO)₅, pointing again to contributions of thermal precursor decomposition.¹²

When such thermal decomposition of FEBID precursors occurs on a surface, it counteracts the spatial selectivity of the deposition process as defined by the electron beam. However, the reactivity of the substrate on which FEBID nanostructures are fabricated can be inhibited by covering the surface with suitable non-reactive adlayers. This has been shown for FEBID from Fe(CO)₅ on the Ag(111) surface under ultrahigh vacuum (UHV) conditions.¹³ While Fe(CO)₅ is decomposed readily by the Ag(111) surface leading to autocatalytic growth (AG) of Fe, a thin adlayer of 2H-tetraphenylporphyrin (2HTPP) molecules suppresses this reaction so that deposition can again be controlled by the electron beam. In this case, a thin seed nanodeposit produced by FEBID from Fe(CO)₅ can initiate further AG.^{14,15} However, the 2HTPP layer as well as several other surfaces that do not induce precursor decomposition in their pristine state can also be converted to a reactive state by electron irradiation. This electron beam induced surface activation (EBISA) process has been demonstrated on diverse materials ranging from oxides and adsorbed layers of large organic molecules to coordination polymers.^{16–18} The surfaces of these materials are activated locally by the focused electron beam to then decompose the precursors Fe(CO)₅ or Co(CO)₃NO dosed via the gas phase after irradiation of the surface. This can again initiate autocatalytic deposit growth akin to a CVD process but restricted to the irradiated area. In the case of Fe(CO)₅, this leads to a deposit, which consists of pure Fe in contrast to the deposits with low Fe content prepared from the same precursor by FEBID.¹⁹

Despite their obvious relevance, the thermal reactions that initiate and sustain autocatalytic deposit growth are often far from understood. They also depend critically on the process conditions such as temperature and pressure regime. This is highlighted, in particular, by various studies on deposit formation from Fe(CO)₅. Aside from the relevance of this precursor to the EBISA studies mentioned above,^{16–18} the surface reactions of Fe(CO)₅ have been investigated by surface science tools under ultrahigh vacuum (UHV) conditions^{20–31} and applied in CVD processes.^{32,33} In

UHV, autocatalytic growth of Fe from Fe(CO)₅ proceeds readily at room temperature on diverse surfaces.^{13,14,16,20–22,34–37} Thermal desorption spectrometry (TDS) of Fe(CO)₅ adsorbed on the Pt(111) surface in UHV has shown that the growth is enabled by desorption of CO leading to an increase of the deposition rate with increasing temperature.^{21,22} In contrast, deposition rates at a Fe(CO)₅ pressure of 0.1 mTorr (rough vacuum conditions) as prevalent in a typical CVD process decreased when the temperature was increased from 200 to 300 °C.³² At 300 °C, the growth was even self-limiting presumably as a result of surface poisoning by decomposition of CO. However, this poisoning could be circumvented by co-flow of NH₃. As an explanation, it was proposed that NH₃ blocks CO adsorption or displaces adsorbed CO from the growing Fe surface.³² On the other hand, CVD from Fe(CO)₅ on oxide surfaces can be inhibited by co-flow of NH₃.³³ In this case, it was proposed that NH₃ blocks acidic surface hydroxyl groups that are held to be involved in decomposition of the precursor. A similar effect was also reported previously for the precursor dicobalt octacarbonyl, Co₂(CO)₈. Here, a co-flow of NH₃ during CVD inhibited deposition on acidic oxide surfaces such as SiO₂ and WO₃.³⁸

The latter type of inhibition would also be of interest for FEBID processes because it could provide a means to suppress unwanted AG of Fe and thus to control deposition exclusively by the electron beam. This would enable an improved spatial selectivity of the deposit formation. However, as NH₃ is efficiently decomposed by electron irradiation,^{39–41} the surface can potentially be reactivated by the use of an electron beam. This would offer the perspective to prepare a nonreactive surface as needed for local activation by EBISA simply by adsorption of NH₃ gas instead of using compounds such as 2HTPP, which must be evaporated at elevated temperatures.¹³ Also, while EBISA allows to grow planar structures by AG in areas predefined by electron irradiation, it would be interesting to be able to stop AG after a certain deposit thickness and reinitiate growth only in the areas that are addressed by the electron beam after adsorption of NH₃. This would enable the fabrication of hierarchical nanostructures based on AG. However, the effect of NH₃ on the surface reactions of Fe(CO)₅ has so far not been investigated under vacuum conditions relevant to FEBID (high vacuum) or in UHV. Also, surfaces that are representative of an actual deposit prepared by FEBID have not yet been studied.

Motivated by these ideas and the present lack of insight into the effect of NH₃ on deposit formation at pressures below typical CVD conditions, we have performed surface science experiments to study the potential inhibition of autocatalytic Fe growth from Fe(CO)₅ by NH₃ and the reactivation of the surface by electron irradiation under UHV conditions. The general approach of the experiments is visualized in Fig. 1. In a first step, an Fe seed deposit was prepared by electron beam induced deposition (EBID). This was done by dosing Fe(CO)₅ onto a supporting Ta surface during electron irradiation from a nonfocused electron gun, which evenly irradiates the entire Ta sheet. This produced a seed deposit all over the Ta surface. The seed deposit was characterized by Auger electron spectroscopy (AES). In the next step, the precursor was dosed without further irradiation and the growth of the deposit by thermal reactions was again monitored by AES. This step was performed either directly on the Fe seed deposit or after

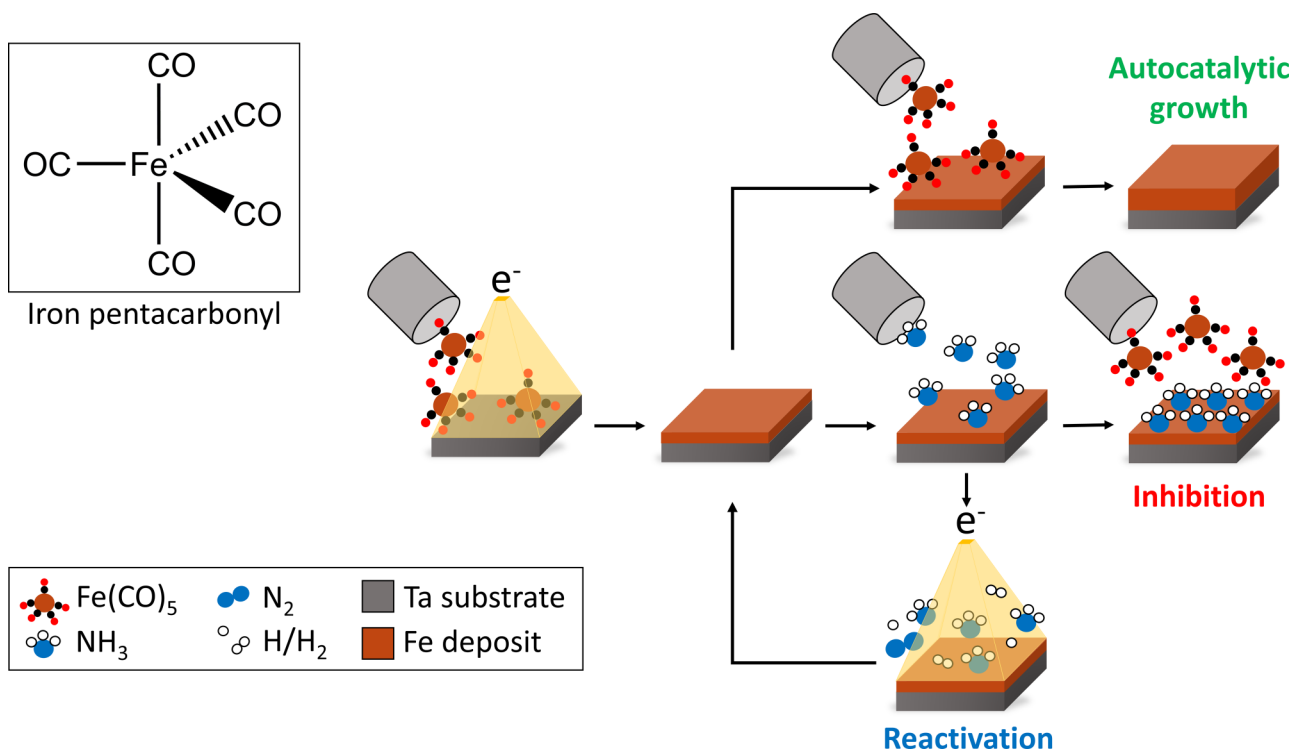


FIG. 1. Molecular structure of iron pentacarbonyl and visualization of the general experimental approach: Fe seed deposits were prepared on a Ta substrate by electron beam induced deposition (EBID) using $\text{Fe}(\text{CO})_5$ as a precursor. Autocatalytic growth (AG) occurred on the Fe seed layer when $\text{Fe}(\text{CO})_5$ was dosed without further irradiation. NH_3 was adsorbed on the Fe seed deposit with the aim of inhibiting AG. NH_3 was removed by electron irradiation to reactivate the surface for further AG.

adsorption of NH_3 on the deposit. Furthermore, we have investigated if NH_3 can be removed again by electron irradiation so that the surface becomes reactivated for further AG of Fe from $\text{Fe}(\text{CO})_5$. In contrast to previous UHV studies, which used single crystal surfaces other than Fe, a particular aim of the present work was also to reveal the reactivity of a surface formed by electron-induced decomposition of $\text{Fe}(\text{CO})_5$, which is representative of an actual FEBID deposit. Considering the low Fe content of such seed layers,¹⁹ the surface reactivity of these deposits was anticipated to differ from that of a pure Fe layer as encountered in CVD³² and also from that of the Pt(111) surface used previously to study the growth of Fe layers in UHV.^{20–22} In addition to the AES experiments, TDS was, therefore, used to characterize the adsorption and reactivity of $\text{Fe}(\text{CO})_5$ on Fe seed layers prepared from $\text{Fe}(\text{CO})_5$ by EBID. The results of this study bear implications toward the development of novel FEBID processes. In particular, the prospects of co-injecting NH_3 during FEBID from $\text{Fe}(\text{CO})_5$ as a viable strategy to suppress unwanted contributions of CVD to deposit formation are discussed.

II. EXPERIMENTAL SECTION

A. UHV setup

All experiments were carried out in an ultrahigh vacuum (UHV) setup with a base pressure of about 10^{-10} mbar, which was

described previously.^{40,42,43} The setup is equipped with a commercial flood gun (SPECS FG 15/40), a quadrupole mass spectrometer (QMS) residual gas analyzer (Stanford, 300 amu), an Auger electron spectrometer (AES) (STAIB DESA 100), and a sputter gun operated with Ar^+ ions. In all experiments, a polycrystalline Ta sheet with a total area of 5 cm^2 was used as a substrate. The entire substrate was exposed to the electron beam during irradiation. The substrate can be cooled by using a liquid nitrogen bath cryostat and warmed up by resistive heating through two thin Ta ribbons spot-welded to the Ta sheet.

B. Sample preparation

Preparation of adsorbed layers was performed based on previously reported procedures.^{40,42} Prior to an experiment, the substrate was sputter-cleaned using Ar^+ ions (3 keV, 30–60 min) to remove any contamination, especially C and O. Cleaning was performed until the underlying AES signals of Ta were clearly visible and signals of C and O had fallen below the noise level. Immediately before precursor deposition, adsorbed volatile compounds from the residual gas were further removed by annealing to 450 K.

The precursor $\text{Fe}(\text{CO})_5$ (Sigma Aldrich, St. Louis, MO, USA, >99.99%) was degassed by repeated freeze–pump–thaw cycles.

NH₃ (Linde, Dublin, Ireland, 99.98%) was used as received. Both compounds were introduced to the vacuum chamber via a gas handling manifold consisting of precision leak valves and a small calibrated volume where the absolute pressure is measured with a capacitance manometer. In each experiment, a calibrated amount of vapor, stated herein as pressure drop in the manifold and quantified as described in Sec. II C, was leaked via a stainless-steel tube with an opening pointing toward the Ta substrate.

EBID layers were prepared by introducing the precursor vapor onto the substrate held at or above room temperature during electron irradiation with an energy of 500 eV and a typical current density of 11 $\mu\text{A}/\text{cm}^2$. Leaking of the precursor was performed within about 2 min for a gas dose corresponding to a pressure drop of 6 mTorr in the gas inlet as applied in most EBID deposition steps. However, the pressure dropped only gradually after the closure of the inlet valve. Irradiation was, therefore, continued until the pressure had approached its value prior to precursor leakage leading to a typical irradiation time of 10 min. This was followed by annealing the substrate to 450 K to remove the remaining intact precursor. Electron doses of an order of 5×10^{16} electrons/ cm^2 were thus applied during an EBID step. To put this into perspective, we note that, in the case of earlier surface science studies on condensed metal carbonyl precursors,^{44,45} such doses were beyond the regime where the rapid loss of CO occurs.

AG experiments were performed at room temperature by leaking the precursor vapor without electron irradiation. Again, the substrate was annealed to 450 K after the AG growth step to remove volatile species. For inhibition experiments, NH₃ was dosed onto the substrate followed by precursor leakage. To study reactivation, the NH₃ adsorbate was irradiated with electrons at 500 eV prior to dosing of the precursor. Electron irradiation was performed until the chamber pressure that increased as a result of electron-stimulated desorption had decayed to an approximately constant level.

C. Thermal desorption spectrometry (TDS)

TDS was performed to characterize the adsorbate thickness obtained upon dosing of vapors at 110 K and to monitor thermal surface reactions of the precursors. After adsorption of the compounds, the substrate was heated at a rate of 1 K/s while monitoring selected m/z ratios over time using the QMS. Each TDS run was followed by a bakeout at 450 K for 30 s. Adsorbate thicknesses were estimated by introducing varying amounts of vapor corresponding to different pressure drops in the gas handling manifold and subsequently observing the evolution of the desorption signals as a function of vapor dose.

The TDS data obtained as a function of vapor dose also allows us to estimate the amount of gas dosed onto the surface during the deposition experiments. As detailed in Sec. III B, the introduction of an amount of gas that corresponds to a pressure drop of about 1 mTorr in the gas inlet leads to saturation of a monolayer of Fe(CO)₅ under cryogenic conditions. Based on a previous estimate of the monolayer surface density of 2.4×10^{14} molecules/ cm^2 (Ref. 24), a gas dose of 1 mTorr, thus, injects roughly this same number of molecules per cm^2 during an EBID or AG step of the experiments described herein.

D. Auger electron spectroscopy (AES)

AES was performed using an electron energy of 5 keV and a pulse counting collection mode accumulating 100 scans from 100 to 800 eV, which takes about 60 min. The spectra shown in Sec. II were acquired using a fixed retarding ratio at variable energy resolution of $dE/E = 0.6\%$. AES data of experiments 2–4 (see Sec. III D and Tables S1 and S2 in the supplementary materials⁴⁶) were recorded in the constant analyzer resolution mode. The beam current measured on the deposits was around 0.3 μA with a beam spot size of the order of 1 mm. This translates to exposures of the order of 10^{18} electrons/ cm^2 during the acquisition of a spectrum. Post-deposition modification of the sample within the area probed by AES is thus likely.⁴⁵ However, further deposition can be neglected because AES was acquired without further precursor dosage. Furthermore, to avoid seeing accumulated surface damage, the spot position was changed after every step (EBID, AG) of sequential experiments.

The AE spectra were used to monitor the deposit composition and growth. Deposit growth was measured as the increase of the three Fe_{LMM} signals. We note that the absolute AES intensities and also the shape of the baseline depends on the resolution mode used in the acquisition of the spectra. Therefore, the intensities of each experimental sequence are referenced to the Ta_{NNN} signal of the freshly sputter-cleaned substrate recorded at the beginning of the individual sequence. We have also attempted to estimate the deposit growth from the attenuation of the two Ta_{NNN} signals using attenuation lengths in Fe of 0.37 nm for electrons with an energy of 167 eV and 0.38 nm at 180 eV derived by interpolation of tabulated values.⁴⁷ In both cases, peak intensities were determined from differential spectra in accord with standard procedures⁴⁸ considering that the signals of the relevant elements are well separated.⁴⁹ The as-acquired direct spectra were subject to a baseline correction using the method of asymmetric least squares after which the first derivative with respect to the electron energy was numerically obtained and subject to a Savitzky–Golay filtering. The peak heights were then obtained from the minimum and maximum of the derivative peak signals. To account for the composition of the deposit, tabulated sensitivity factors were applied.⁴⁸

III. RESULTS AND DISCUSSION

A. Preparation of Fe seed deposits by electron beam induced deposition (EBID)

The deposition of Fe on the Ta substrate by EBID and the subsequent AG on the Fe EBID deposit were monitored by AES. In such experiments, the deposit thickness must not exceed the escape depth of Auger electrons from the underlying Ta substrate to ensure that information on the deposit growth can be deduced. Therefore, the dependence of the AES signal intensities on the amount of Fe(CO)₅ gas dosed during the EBID process was investigated first (Fig. 2). For illustration, we include both the measured direct spectra [Fig. 2(a)] and the differentiated data [Fig. 2(b)], the latter being used to quantify the intensities as peak-to-peak heights. The substrate shows only the expected Ta_{NNN} signal (167 and 180 eV) and a small O_{KLL} signal at 513 eV that points to some surface oxidation. In contrast, the data acquired after dosing of

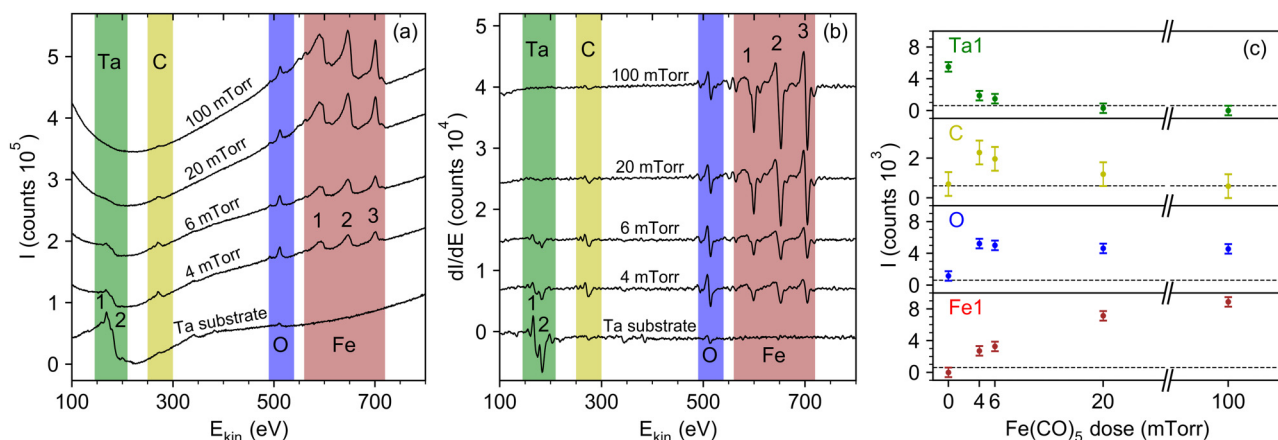


FIG. 2. (a) AES recorded on a Ta substrate and on Fe deposits prepared by electron exposure (500 eV) during dosing of different amounts of $\text{Fe}(\text{CO})_5$ at 400 K. The gas doses are denoted as pressure drops in the volume from which the gas was leaked. Each deposition was performed on the freshly sputtered Ta substrate and was followed by subsequent annealing to 450 K. (b) Differentiated AES data from (a). (c) Intensity of the characteristic Auger signals as a function of $\text{Fe}(\text{CO})_5$ dose obtained from (b) as described in Sec. II D. The horizontal dashed lines mark the detection limits. Detection limits and vertical error bars were derived from the peak-to-peak height of the noise level within the differential AES data. Note that the intensities have not been corrected by sensitivity factors because the different elements are not homogeneously distributed within the probed depth. For clarity, the spectra in (a) and (b) are offset in the vertical direction.

$\text{Fe}(\text{CO})_5$ during simultaneous 500 eV electron irradiation at a substrate temperature of 400 K exhibit the expected Fe_{LMM} signals at 592, 651, and 704 eV [Figs. 2(a) and 2(b)]. Their intensity increases with the amount of dosed $\text{Fe}(\text{CO})_5$, while the Ta_{NNN} signal is attenuated and drops to baseline levels for a gas dose corresponding to a pressure drop of 100 mTorr in the gas inlet system [Fig. 2(c), green, top].

At 20 mTorr, the Ta signal has nearly disappeared indicating that Auger electrons originating from the substrate are completely screened at larger deposit thickness. This attenuation also accounts for the relatively small increase of the Fe_{LMM} signals when the $\text{Fe}(\text{CO})_5$ dose is increased from 20 to 100 mTorr [Fig. 2(c), red, bottom], which indicates that at the largest deposit thickness, only the upper part of the deposit is monitored by AES. Therefore, overall gas doses below 20 mTorr were applied in all subsequent experiments. We note that EBID performed using the same amount of gas without heating the substrate yielded a less intense Fe_{LMM} signal than when the substrate was heated to 400 K (see Fig. S1 in the supplementary material⁴⁶). Therefore, a gas dose that yields a sufficiently thin deposit at 400 K will also be suitable for EBID experiments performed near room temperature.

Interestingly, the C_{KLL} Auger signal (271 eV) decreases with increasing deposit thickness for $\text{Fe}(\text{CO})_5$ doses above 4 mTorr [Fig. 2(c), yellow, second from top] despite the fact that all deposits shown in Fig. 2 were prepared by EBID which typically yields a material that contains residual elements from the CO ligands.¹⁹ We ascribe this increase of the deposit purity with thickness to a contribution of AG to deposit formation that becomes more efficient when a sufficient amount of seed material has formed on the Ta substrate (see also Sec. III C). On the other hand, a persistent O_{KLL} signal is more or less independent of the deposit thickness [Fig. 2(c), blue, second from bottom]. This suggests again that not

only the incorporation of oxygen from the CO ligands but also surface oxidation by residual H_2O in the vacuum chamber after preparation of the deposit contributes to the O_{KLL} signal. This latter process is likely to result from electron-induced surface chemistry during the acquisition of the AES data.

Based on the attenuation of the AES Ta_{NNN} signal, the procedure described in Sec. II D would imply a deposit thickness of 0.40 nm after a gas dose of 4 mTorr. After 6 and 20 mTorr, values of 0.42 and 1.04 nm, respectively, are obtained. As the experiments to be described in Sec. III D aim at monitoring the deposit growth during AG steps, it is important to reflect first upon the validity of these thickness values. In fact, a layer thickness derived from the attenuation of the AES Ta_{NNN} signal as summarized in Sec. II D is not a priori reliable because the calculation assumes a homogeneous thickness over the entire probed area. This is not necessarily the case when deposition is performed at a temperature that enables surface diffusion of the precursor molecules. Diffusion leads to aggregation of the material as reported, for instance, for dot deposits prepared from $\text{Fe}(\text{CO})_5$ on SiO_2 . In this case, a dot consisted of several well separated aggregates.¹⁹ A similar situation is quite likely for the present seed deposits because EBID was also performed at or above room temperature. Furthermore, most experiments applied an amount of precursor vapor that corresponds to a pressure drop of 6 mTorr in the gas inlet (see Secs. III C and III D). According to our TDS results, this translates to an average layer thickness of roughly six monolayers (see Secs. III B and III C). Under the condition that molecules become immobilized at the site where they impinge on the surface, a simple statistical model suggests that approximately an average thickness of five to six monolayers is needed to completely cover the underlying surface.⁵⁰ When EBID is performed at room temperature, i.e., above the desorption temperature of $\text{Fe}(\text{CO})_5$ multilayers

(see Sec. III B), less material will remain on the surface. Also, the molecules are anticipated to be mobile enough to aggregate. The seed layers prepared herein by EBID are, therefore, unlikely to cover the entire Ta substrate.

In this situation, a thickness calibration based on the attenuation of the AES Ta_{NNN} signal must be regarded with caution. The attenuation length of Ta_{NNN} Auger electrons of 0.37 nm⁴⁷ suggests that already one monolayer of Fe with a reported thickness of 0.2 nm⁵¹ attenuates the signal by 42%, two monolayers would lead to an attenuation of 66%. In the extreme case that the material aggregates during deposition to form multilayer islands, Auger electron emission from the uncovered surface would dominate the AES Ta_{NNN} signal. In this scenario, a decrease of the Ta_{NNN} signal implies that an increasing fraction of the surface is covered by the aggregates. This is conceivable because thermal growth will most likely increase both the height and the width of a seed deposit. Based on this model, the attenuation of the Ta_{NNN} signal observed after EBID with a gas dose of 20 mTorr thus would imply that about 6% of the surface remain void of deposit. Of course, it is likely that a realistic scenario would contain both a fraction of non-covered surface as well as deposited agglomerates that do not fully screen Auger electrons from the Ta substrate. Therefore, the

increase of the Fe_{LMM} signals referenced to the Ta_{NNN} signal of the freshly sputter-cleaned Ta substrate in each experiment will be used as an alternative measure of the deposit growth as described in Sec. III D. Furthermore, we refer to the thickness values derived from the attenuation of the Ta_{NNN} signal as an apparent thickness.

The four main deposition experiments of the present study with an overall number of 11 EBID seed deposits and their analysis in terms of deposit growth are discussed in Sec. III D. The corresponding AES intensities and apparent thickness values are included in Tables S1 and S2 in the supplementary material.⁴⁶ We note here that due to fluctuations of the absolute AES intensities and different baseline shapes, the Fe_{LMM} to Ta_{NNN} intensity ratios also varied between the four experiments. It is, therefore, not possible to draw a direct comparison between all EBID deposits based on the absolute Fe_{LMM} intensities. However, within individual experiments that were each performed over a time span of about one week, the repeated preparation of EBID seed layers produced results that are of a comparable order of magnitude. Some variation of the EBID seed layers between individual depositions within each experiment as summarized in Tables S1 and S2 as well as Fig. S11 in the supplementary material⁴⁶ most likely relates to the fact that Fe(CO)₅ gas flow during leaking was not precisely constant because

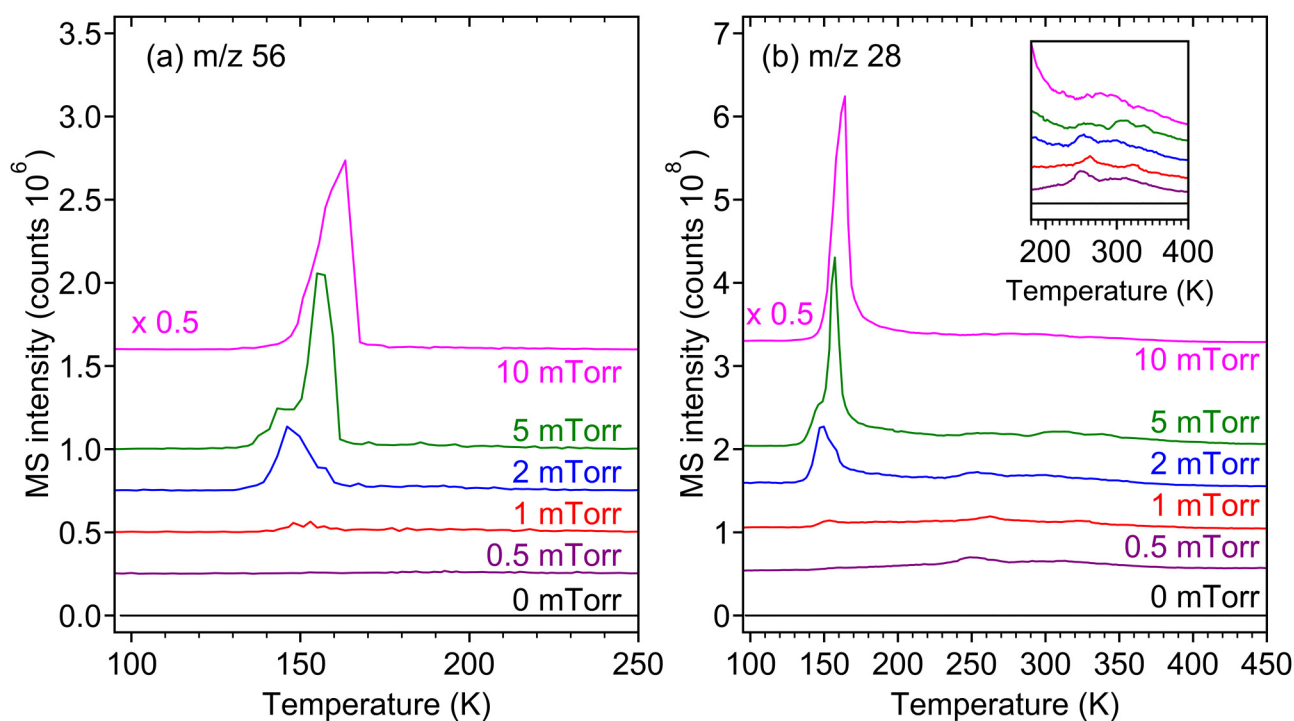


FIG. 3. Thermal desorption spectra (TDS) of Fe(CO)₅ on a Fe EBID deposit recorded at (a) m/z 56 and (b) m/z 28. For better visualization, the scale in (a) is limited to 250 K because further desorption signals at higher temperature are absent. The amount of Fe(CO)₅ that was dosed in the individual experiments is stated as a pressure drop in the gas inlet system during leaking of the gas. 0 mTorr denotes a control TDS experiment without dosing Fe(CO)₅. The EBID deposit was prepared prior to the TDS experiments by simultaneous electron irradiation (500 eV) and dosing of an amount of Fe(CO)₅ that corresponded to a pressure drop of 6 mTorr in the gas inlet system with the substrate held at 400 K. The data obtained after adsorption of Fe(CO)₅ on the Ta substrate were acquired in the sequence 5, 1, 10, 2, 0.5 mTorr. Each TDS run was terminated by a 30 s bakeout at 450 K. For clarity, the TDS curves are offset in the vertical direction.

it was controlled by manual operation of a simple UHV valve. For constant electron current density during leaking, this implies a nonconstant ratio of electron and precursor flux, which rationalizes the observed variations of the EBID layer thickness. However, as will be shown in Sec. III D, the overall trends regarding AG on the EBID seed deposits are reproduced over all experiments.

B. Adsorption of $\text{Fe}(\text{CO})_5$ on Fe seed deposits prepared by EBID

While adsorption and thermal surface reactions of $\text{Fe}(\text{CO})_5$ on various metals and, in particular, on single crystal metal surfaces have been investigated previously,^{20,23–31} surface science studies of the adsorption of $\text{Fe}(\text{CO})_5$ on an actual FEBID deposit are so far nonexistent. Aiming at fundamental insight into the possible thermal surface chemistry involved in FEBID and in the conditions that allow for subsequent AG processes,^{13–19} we have, therefore, performed TDS for $\text{Fe}(\text{CO})_5$ adsorbed on Fe deposits prepared by EBID and compare the data to results obtained on other surfaces.

First, an Fe EBID seed layer was prepared on a freshly sputtered Ta substrate held at 400 K. This was done by dosing $\text{Fe}(\text{CO})_5$ onto the surface during electron irradiation with an energy of 500 eV. For this preparation, the amount of $\text{Fe}(\text{CO})_5$ gas leaked into the vacuum chamber corresponded to a pressure drop of 6 mTorr in the gas inlet system. After deposit formation, the substrate was cooled to 100 K for adsorption of further $\text{Fe}(\text{CO})_5$ and thermal desorption experiments. Figure 3 shows TDS data at m/z 28 ($\text{CO}^+/\text{Fe}^{2+}$) and m/z 56 (Fe^+) recorded from the same seed deposit but for different amounts of $\text{Fe}(\text{CO})_5$.

Similar results were obtained for a dose corresponding to 2 mTorr (see Fig. S2 in the supplementary material⁴⁶). At low amounts of adsorbed gas, the m/z 56 TDS data [Fig. 3(a)], which represent the desorption of volatile Fe-containing species and, in particular, intact $\text{Fe}(\text{CO})_5$ (see further on), first show a desorption signal at 150 K. This signal starts to appear for a gas dose corresponding to a pressure drop of 1 mTorr and evolves into a continuously increasing peak with a maximum at 165 K. The same behavior was also observed upon adsorption of $\text{Fe}(\text{CO})_5$ on the underlying Ta substrate as well as on Fe layers prepared by further AG as described in Sec. III C (see Figs. S3 and S4 in the supplementary material⁴⁶). These m/z 56 signals fall within the temperature range of multilayer desorption of $\text{Fe}(\text{CO})_5$ as observed on different single crystal metal surfaces.^{20,21,23–26,31,52,53} However, while multilayer desorption with a double peak that increased with coverage was also observed on Si(111),²³ the shift of the $\text{Fe}(\text{CO})_5$ multilayer desorption to higher temperature has not been described before to the best of our knowledge. This type of thickness dependence of the TDS data was observed previously for hexamethyldisiloxane.⁵⁴ In this case, the shift to higher desorption temperature was ascribed to a transition from a disordered to a more ordered phase that only occurs when a sufficient film thickness is reached. A crystallization that only occurred at a sufficient surface coverage has also been reported for benzene.^{55,56} We propose that a similar phase transition is observed here for $\text{Fe}(\text{CO})_5$.

In contrast to the sharp multilayer desorption signal, a monolayer signal is very weak in the m/z 56 TDS data [Fig. 3(a)]. Monolayer desorption has been typically observed within 10–30 K

above the multilayer signal on different metal surfaces^{20–26,28,29,31,53} but is hardly discernible here. The appearance of the multilayer desorption signal for a gas dose of 1 mTorr as seen in the combined TDS data of Fig. 3 and Figs. S2–S4 of the supplementary material,⁴⁶ thus, indicates saturation of the monolayer regime. The absence of a monolayer desorption signal points to dissociative adsorption within the monolayer regime. In line with this, the m/z 28 TDS curves [Fig. 3(b)] do not simply reflect the m/z 56 data which represent the Fe^+ fragment of $\text{Fe}(\text{CO})_5$ produced in the QMS but show additional broad desorption signals extending from 170 to 400 K already for the lowest $\text{Fe}(\text{CO})_5$ dose [see the inset of Fig. 3(b)]. Based on the missing m/z 56 signals in this temperature range, the additional m/z 28 signals are assigned exclusively to CO^+ . Supported by the absence of CO desorption in a control TDS recorded without prior dosing of $\text{Fe}(\text{CO})_5$ [Fig. 3(b), denoted as 0 mTorr], this gives evidence of dissociative adsorption of monolayer $\text{Fe}(\text{CO})_5$ on the Fe deposit as also deduced previously from the fact that AG occurs on Fe seed layers produced by FEBID^{14,16}

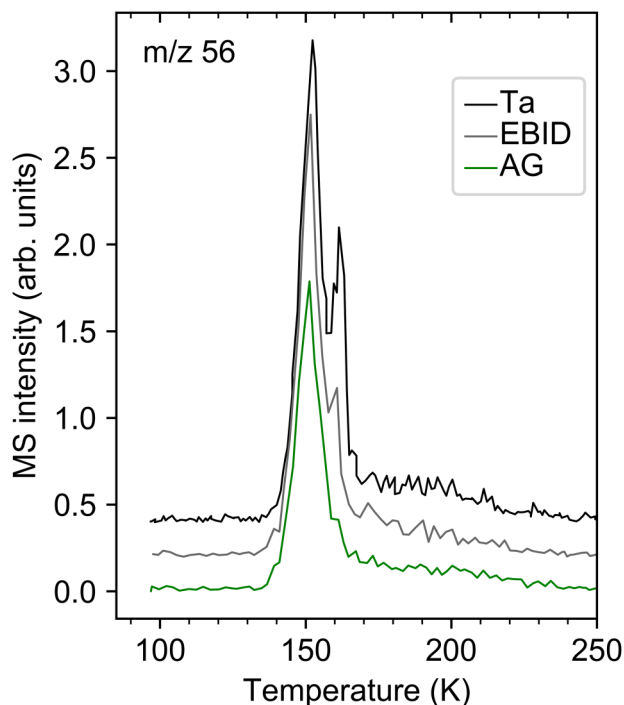


FIG. 4. Thermal desorption spectra (TDS) recorded at m/z 56 after dosing 2 mTorr of $\text{Fe}(\text{CO})_5$ on the freshly sputtered Ta substrate (black, top), on a Fe EBID deposit prepared by dosing 2 mTorr $\text{Fe}(\text{CO})_5$ during electron irradiation (500 eV) at 400 K (gray, middle), and on an Fe layer produced by AG during threefold dosing of 2 mTorr $\text{Fe}(\text{CO})_5$ [total dose 6 mTorr, the continuous growth of the deposit is demonstrated by AES data shown as Fig. S5 in the supplementary material (Ref. 46)] on an EBID deposit prepared again by dosing 2 mTorr $\text{Fe}(\text{CO})_5$ during electron irradiation (500 eV) (green, bottom). The amount of $\text{Fe}(\text{CO})_5$ that was dosed in the individual experiments is stated as a pressure drop in the gas inlet system during leaking of the gas. For clarity, the TDS curves are offset in the vertical direction.

and in line with the very weak monolayer desorption signal of intact $\text{Fe}(\text{CO})_5$ [Fig. 3(a)]. A distinct CO desorption state at 330 K has, for instance, been observed after adsorption of $\text{Fe}(\text{CO})_5$ on $\text{Ag}(111)$.^{24,26} This signal, which significantly gained intensity after electron irradiation at 90 K,²⁴ was assigned to $\text{Fe}_x(\text{CO})_y$ species.^{24,26} While such species are likely intermediates during the EBID step, they must already have decayed in the present experiment during the annealing at 450 K after deposition. This supports that the CO desorption seen above 170 K in Fig. 3(b) results from thermal surface reactions that dissociate CO from the precursor $\text{Fe}(\text{CO})_5$ on the EBID layer. This process has been studied in depth on $\text{Pt}(111)$ where it was shown that desorption of CO liberates binding sites on the surface which, in turn, increases the rate of thermal Fe deposition during dosing of $\text{Fe}(\text{CO})_5$.^{20–22} In analogy, the CO desorption signals below 300 K [the inset of Fig. 3(b)] rationalize the autocatalytic growth of Fe deposits at room temperature as described in Sec. III C. Overall, the fact that CO desorption from intermediates that are chemisorbed on an EBID layer already occurs below room temperature also explains why such Fe seed layers efficiently induce AG from $\text{Fe}(\text{CO})_5$ as observed previously in FEBID processes performed in UHV.^{13–19}

We note that the shape of the m/z 28 desorption signals above 170 K varies somewhat from one TDS run to the next [Fig. 3(b)]. Dissociative adsorption was previously observed on other surfaces such as $\text{Ag}(111)$,^{24,26} $\text{Pt}(111)$,^{20–22} $\text{Pd}(111)$,²⁵ and $\text{Ru}(001)$,³¹ while adsorption on $\text{Si}(111)$ ²³ and $\text{Au}(111)$ ⁵³ is nondissociative. Consultation of these previous results shows that CO desorption following dissociative adsorption depends critically on the binding to the metal surface. In line with this, the shapes of the TDS signals above 170 K as shown in Fig. 3(b) are distinctly different from the m/z 28 TDS data for the different single crystal surfaces.^{20,21,23–26,31,52,53} Therefore, we relate the slight variations observed in the shape of the m/z 28 monolayer desorption signals between the different coverages seen in Fig. 3(b) to changes in the composition of the surface. Such changes result from the thermal decomposition of the $\text{Fe}(\text{CO})_5$ adsorbate upon temperature increase during the previous TDS experiment. However, we have judged this effect as not pronounced enough to call for a more detailed study.

The CO desorption signals above 170 K were also found to be similar to those seen in Fig. 3(b) when the experiment was performed on a thinner EBID layer, directly on the sputtered Ta

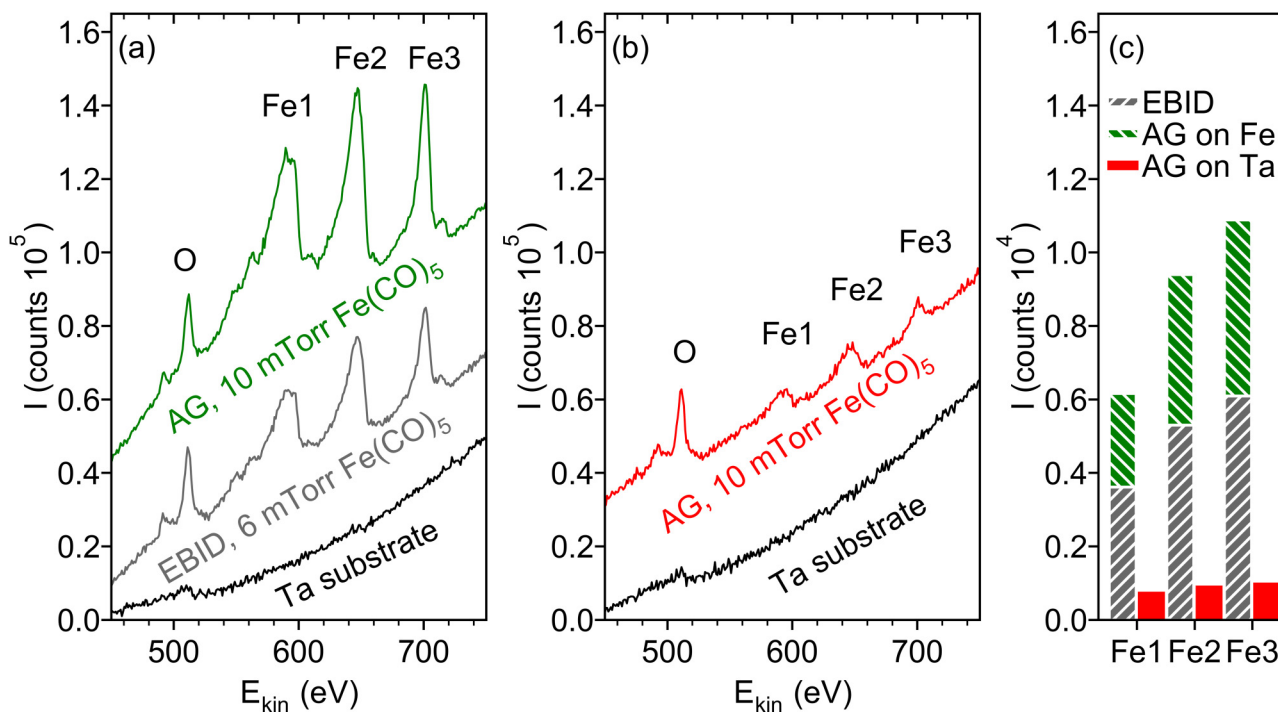


FIG. 5. (a) AES in the range of the Fe_{LMM} signals (Fe1 at 592 eV, Fe2 at 651 eV, Fe3 at 704 eV) recorded on the freshly sputtered Ta substrate (black, bottom), the same surface after simultaneous electron irradiation (500 eV) and dosing of a defined amount of $\text{Fe}(\text{CO})_5$ gas at 400 K followed by annealing to 450 K (EBID, dose denoted as pressure drop in the volume from which the gas is leaked, gray, middle), and after further dosing of $\text{Fe}(\text{CO})_5$ without electron exposure at room temperature and again a subsequent annealing step to 450 K (green, top). (b) AES of the Ta substrate before (black, bottom) and after dosing of $\text{Fe}(\text{CO})_5$ without electron irradiation at room temperature followed by annealing to 450 K (red, top). (c) Increase of the Fe_{LMM} signals during the deposit growth steps shown in (a) and (b). Note that the Fe_{LMM} intensities are exceptionally not referenced to the Ta_{NIN} signal of the clean Ta substrate because the total AES intensities were comparable in the two experiments. The same amount of $\text{Fe}(\text{CO})_5$ yields much less Fe on the Ta surface than on a previous Fe deposit. For clarity, the spectra in (a) and (b) are offset in the vertical direction.

substrate, or on an Fe layer deposited by AG (see Figs. S2–S4 in the supplementary material⁴⁶). This indicates that thermal surface reactions occur on all of these surfaces. However, Fig. 4 compares TDS data obtained from Fe(CO)₅ adsorbed on Ta, on an Fe deposit prepared by EBID, and on a deposit prepared by AG. Here, the highest intensity of the 165 K multilayer signal and, thus, the highest recovery of intact Fe(CO)₅ are observed on Ta and the least on the AG deposit. This indicates that thermal dissociation of Fe(CO)₅ is more efficient on an Fe deposit prepared by EBID than on Ta and even more efficient on a deposit prepared by AG. This is also reflected in the amount of deposit growth as demonstrated next (Sec. III C).

C. Autocatalytic growth of Fe on seed deposits prepared by EBID

The next set of experiments aimed at establishing that dissociative adsorption of Fe(CO)₅ on deposits prepared from EBID as deduced from TDS (Sec. III B) in fact leads to autocatalytic growth of Fe under the given experimental conditions. To this end, Fe(CO)₅ was dosed onto an Fe seed deposit at room temperature without electron irradiation. The results are shown in Fig. 5. Each

deposition experiment was performed on the freshly sputtered Ta substrate which had been cleaned until all signals other than Ta_{NNN} were absent in AES [black, bottom curve in Fig. 5(a)]. First, an Fe seed deposit was prepared by dosing a fixed amount of Fe(CO)₅ onto the Ta substrate held at 400 K during electron irradiation at 500 eV. This led to clearly visible Fe_{LMM} signals [gray, middle curve in Fig. 5(a)]. These signals increased again when further Fe(CO)₅ was dosed onto the thus obtained Fe seed layer without electron irradiation [green, top curve in Fig. 5(a)]. The O_{KLL} signal points to some incorporation of ligand material into the deposit or again to oxidation by residual H₂O from the chamber background. This signal did not increase together with the Fe signals during the AG step pointing to higher purity of the AG layer as compared to the Fe seed deposit. This is in line with the high Fe purity observed previously in UHV FEBID and AG experiments.^{14,16,19}

For comparison, AG was also attempted on the freshly sputtered Ta substrate in a separate experiment. Here, we used the same amount of Fe(CO)₅ as in the AG step of the previous experiment. In contrast to the result for the Fe EBID seed layer [Fig. 5(a)] and in line with the TDS results (Fig. 4), deposition of Fe is less efficient on the Ta substrate itself as evident from the low intensity of the Fe_{LMM} signals [red, top curve in Fig. 5(b)]. This is also visualized

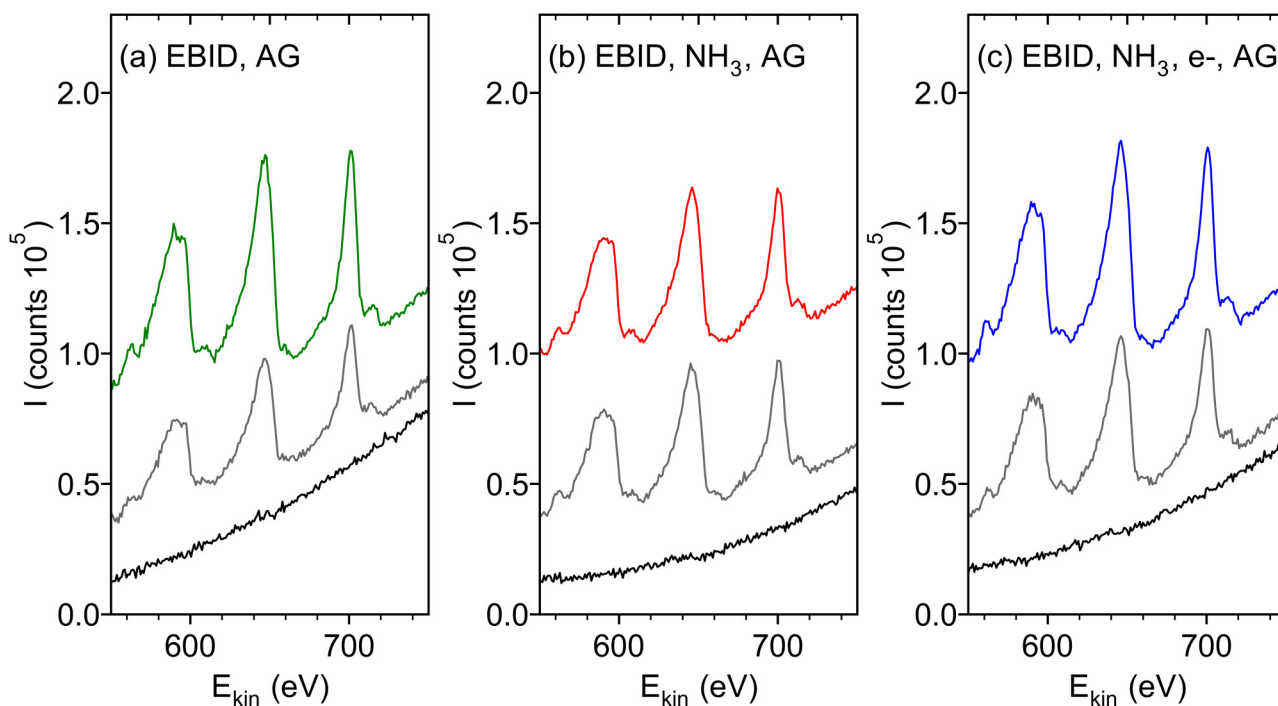


FIG. 6. (a) AES in the range of the Fe_{LMM} signals (Fe1 at 592 eV, Fe2 at 651 eV, Fe3 at 704 eV) recorded on the freshly sputtered Ta substrate (black, bottom), on the same surface after simultaneous electron irradiation (500 eV) and dosing Fe(CO)₅ gas at 400 K followed by annealing to 450 K (EBID, dose corresponding to a pressure drop of 6 mTorr in the volume from which the gas is leaked, gray, middle) and after further AG of Fe by dosing Fe(CO)₅ (10 mTorr) without electron exposure at room temperature followed again by annealing to 450 K (green, top). (b) AES data from an analogous experiment but with NH₃ (20 mTorr) dosed at room temperature onto the EBID Fe layer prior to the AG step (Ta shown in black on bottom, the EBID layer shown in gray in middle, the AG layer shown in red on top). (c) AES data from an analogous experiment but with NH₃ (20 mTorr) dosed at room temperature onto the EBID Fe layer followed by further electron irradiation (500 eV) prior to the AG step (Ta shown in black on bottom, the EBID layer shown in gray in middle, the AG layer shown in blue on top). For clarity, the spectra are offset in the vertical direction.

in Fig. 5(c), which compares the intensity increase of the three Fe_{LMM} signals during EBID (gray, hatched bottom bar) and AG on the thus obtained Fe seed layer (green, hatched top bar) as well as directly on the Ta substrate (red, solid bar). This gives clear evidence that AG of Fe occurs predominantly on the Fe seed layer prepared by EBID but only to a minor extent on a sputtered Ta surface. We note that the apparent thickness of the deposits as estimated from the attenuation of the Ta_{NNN} signal (see Sec. II D) amounts to 0.41 nm after the EBID step, 0.60 nm after AG on the EBID layer and to 0.22 nm after an AG experiment on the Ta substrate. The increase of the apparent deposit thickness during AG is comparable to an Fe monolayer which has a thickness near 0.2 nm.⁵¹ This indicates that both on the EBID layer and on the Ta substrate, AG leads to a deposit with thickness in the monolayer regime, in striking contrast to the much more pronounced increase of the Fe_{LMM} signals on the EBID layer. The relative intensities of the Fe_{LMM} and O_{KLL} signals, however, reveal that the material deposited on Ta contains a significantly higher amount of oxygen [Fig. 5(b)] and also carbon (see Fig. S6 in the supplementary material⁴⁶) as compared to Fe than both the EBID layer and the layer resulting from AG on the latter [Fig. 5(a)]. Considering that the sensitivity factors of the peaks are of similar order of magnitude [1.10 for O_{KLL} (513 eV) versus 0.76 for Fe_2 (651 eV), i.e., the second Fe_{LMM} signal],⁴⁸ we propose that CO released as a

consequence of thermal decomposition of $Fe(CO)_5$ contributes to the attenuation of the Ta signal on the substrate itself and impedes the growth of a thicker Fe layer.

D. Inhibition of AG by adsorbed NH_3 and reactivation by electron exposure

The effect of NH_3 on the AG of Fe from $Fe(CO)_5$ was studied in three separate experiments on deposits prepared by EBID as described in Sec. III A. An additional experiment was performed on a deposit after the first AG step. As detailed in Secs. II D and III A, the efficiency of AG was evaluated from the increase of the Fe_{LMM} signals in AES referenced to the Ta_{NNN} signals of the freshly sputtered Ta substrate (Table S1 of the supplementary material⁴⁶). In addition, an apparent deposit thickness was determined from the attenuation of the Ta_{NNN} AES signals (Table S2 of the supplementary material⁴⁶) as described in Sec. II D and explained further in Sec. III A. Full range AES data for all experiments are also presented in Figs. S7–S10 of the supplementary material⁴⁶.

Figure 6 shows representative results obtained from EBID deposits that were each prepared from the same amount of $Fe(CO)_5$ on the freshly sputtered Ta substrate held at 400 K (Experiment 1 in Tables S1 and S2 of the supplementary material⁴⁶). The increase of the Fe_{LMM} intensity during the AG steps of

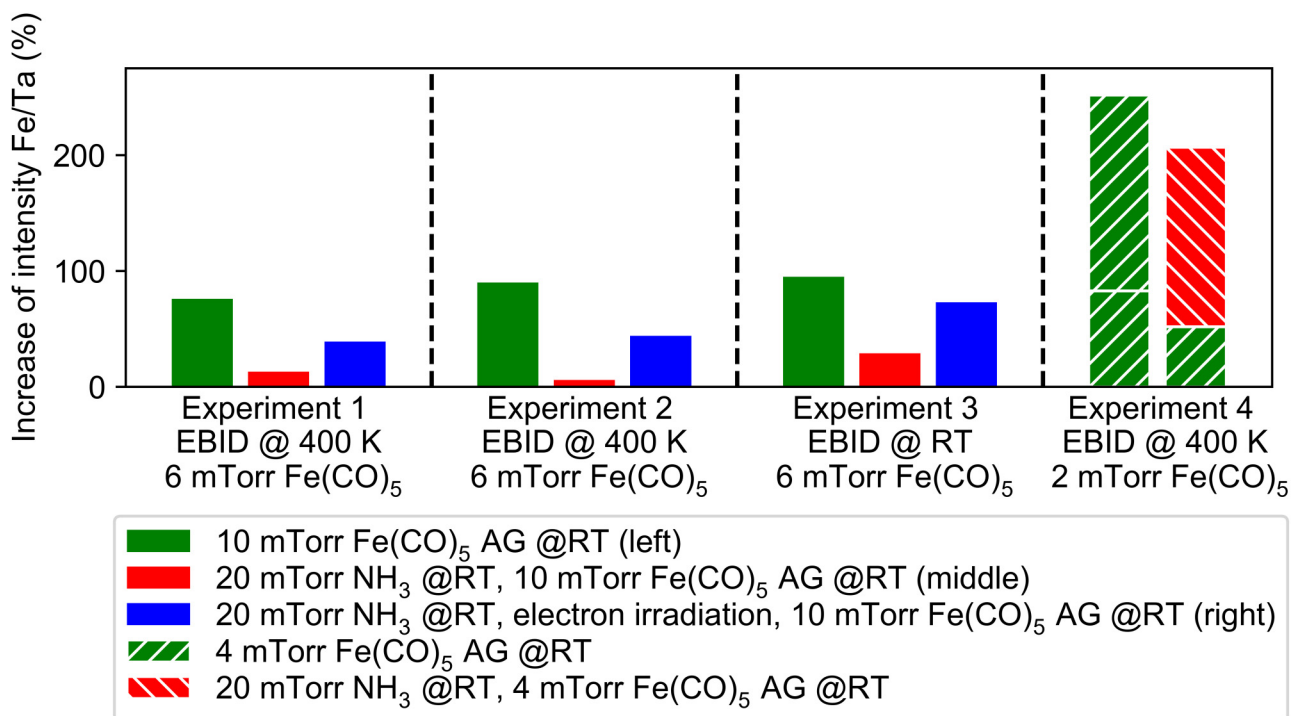


FIG. 7. Deposit growth during the AG step of experiments 1–4 stated as the increase of the Fe_{LMM} AES signals as compared to the same intensity obtained from the underlying EBID Fe layer. All Fe_{LMM} AES signals were referenced to the Ta_{NNN} signals of the freshly sputtered Ta substrate prior to each deposition sequence. The AES intensities used to derive the data shown herein are presented in Table S1 of the supplementary material (Ref. 46). For experiment 4, the divided bars denote the increases during the two sequential AG steps. RT denotes that the experiment was performed at room temperature.

experiment 1 is also summarized in the leftmost entry of Fig. 7. In addition, the increase of the apparent deposit thickness is shown as the leftmost entry of Fig. 8. For reference, AG was first performed by leaking further 10 mTorr of $\text{Fe}(\text{CO})_5$ directly on the EBID Fe layer [Fig. 6(a)]. This led to an increase of the Fe_{LMM} signals by 76% (see Fig. 7), while the apparent thickness increased by roughly 46% as compared to that of the initial EBID layer (see Fig. 8). In contrast, AG was less efficient when NH_3 was adsorbed on the EBID layer leading to a much smaller increase of the Fe_{LMM} signals as compared to the EBID layer [Figs. 6(b) and 7] and a mere 13% increase of the apparent deposit thickness during the AG deposition step (Fig. 8). In a third deposition sequence, the surface was reactivated by electron irradiation with an energy of 500 eV following adsorption of NH_3 [Fig. 6(c)]. This led again to a more pronounced increase of the Fe_{LMM} signals albeit somewhat less than observed directly on the EBID layer (see Fig. 7). Here, the apparent thickness increased again by 49% during the AG step (Fig. 8). The overall result indicates that NH_3 counteracts AG of Fe from $\text{Fe}(\text{CO})_5$ but the deposit can be reactivated by electron irradiation.

Experiment 2 was a repetition of experiment 1 which performed the EBID step with the substrate being held at 400 K. In contrast, the substrate was not heated during EBID in experiment 3 (see Tables S1 and S2 in the supplementary material⁴⁶). The results

confirm the trend that adsorption of NH_3 on the Fe layer prepared by EBID decreases the growth rate in the AG step but that electron irradiation of adsorbed NH_3 can reestablish AG (Figs. 7 and 8). This general trend holds despite the fact that the intensity of the Fe_{LMM} signals and the apparent deposit thickness after the EBID step varied somewhat between the individual deposition sequences (see Sec. III A, Table S1 and S2 as well as Fig. S11 in the supplementary material⁴⁶).

The fact that both Fe_{LMM} AES signals referenced to the Ta_{NNN} signals of the freshly sputtered Ta substrate (Fig. 7) as well as the apparent deposit thickness (Fig. 8) increased to a similar amount during AG in all deposition sequences in absence of NH_3 suggests that the active surface scales linearly with the amount of material deposited in the EBID step. Considering that an Fe monolayer has a thickness near 0.2 nm,⁵¹ the attenuation of the Ta_{NNN} signals by the present EBID layers would imply coverages ranging between 1 and 2.5 monolayers (Fig. S11 in the supplementary material⁴⁶) based on the assumption of a homogeneous thickness. However, we observe a linear scaling of the increase of the apparent thickness during AG with the initial EBID layer apparent thickness (Fig. 9). As discussed in Sec. III A, this confirms our assumption that the apparent thickness in fact relates to an increased surface density of Fe seed particles and a concomitant decrease of the remaining free Ta surface.

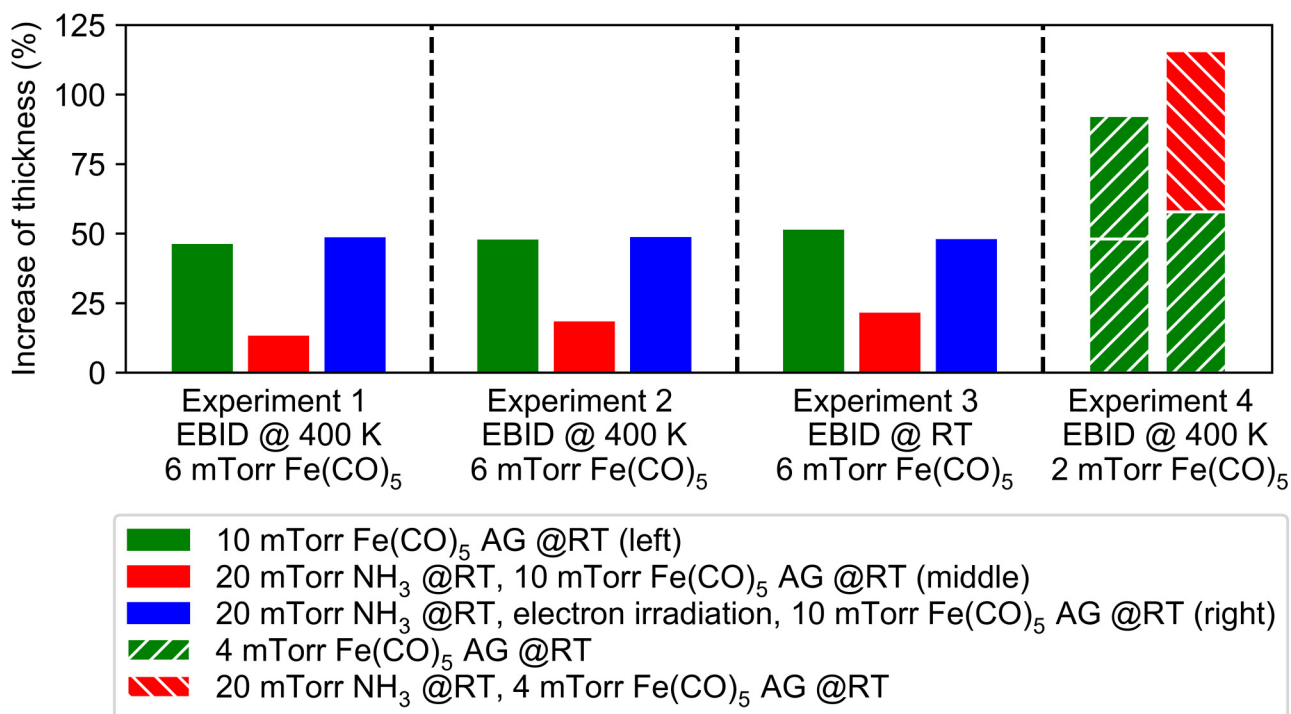


FIG. 8. Deposit growth during the AG step of experiments 1–4 stated as relative apparent thickness increase of the Fe deposit as compared to the apparent thickness of the underlying EBID Fe layer. Absolute values are presented in Table S2 and Fig. S11 of the supplementary material (Ref. 46). For experiment 4, the divided bars denote the increases during the two sequential AG steps. The apparent thickness of the deposit represents the value deduced from the attenuation of the Ta_{NNN} signals as described in Secs. II D and III A. RT denotes that the experiment was performed at room temperature.

The similar AG rates on the pristine and the reactivated EBID Fe layers point to efficient removal of NH_3 by electron irradiation. Previous studies have in fact described the electron-induced conversion of NH_3 to N_2 by the release of hydrogen.^{40,57–60} We propose that such reactions are also operative in the present case. AES of the deposit recorded after adsorption of NH_3 and subsequent electron irradiation supports this view because the spectrum does not reveal an N_{KLL} signal that would be expected at 389 eV.⁴⁸ This result indicates that NH_3 is in fact decomposed to volatile species instead of being incorporated in the Fe deposit as nitride. Nitridation by the use of NH_3 is a common process to improve the properties of metals that aims, for instance, at improved surface hardness and other mechanical properties.⁶¹ Its efficiency depends on the branching ratio between incorporation of nitrogen into the Fe lattice and nitrogen surface diffusion or recombination.⁶² A study based on combined density functional theory (DFT) and kinetic Monte Carlo (kMC) calculations revealed that the highest energy barrier relates to the nitrogen penetration step into the Fe lattice while the barrier for dissociation of NH_3 on the surface is considerably smaller.⁶² In consequence, nitridation is typically a high temperature process.^{62–64} Under the conditions used in the

present study and in FEBID processes, namely, electron irradiation of the deposit near room temperature, nitrogen-containing species released by electron-induced dissociation of NH_3 are more likely to remain on the surface to eventually yield N_2 , which can readily desorb. This rationalizes the lack of the N_{KLL} signal seen in Fig. 10 and in the AES data of experiments 1–4 (see Figs. S7–S10 in the supplementary material⁴⁶).

Experiment 4 was performed to investigate the effect of NH_3 on a deposit prepared by AG from $\text{Fe}(\text{CO})_5$ instead of directly on the EBID layer. In this experiment, a first AG step was performed after the EBID step and prior to dosing of NH_3 . This was followed by a second AG step. For comparison, the second AG step was performed on the first AG layer without dosing of NH_3 (see also Tables S1 and S2 in the supplementary material⁴⁶). The complete AES data is presented in Fig. S10 of the supplementary material,⁴⁶ but the summary of the result is again included in Figs. 7 and 8. Clearly, the growth during the second AG step is rather similar in the deposition sequences with and without NH_3 . Dosing of NH_3 onto a previous AG layer does not inhibit AG from $\text{Fe}(\text{CO})_5$ in the same manner as on the deposit prepared by EBID. Recalling that the AG layer has a higher purity than a deposit prepared by EBID, we propose that the impurity species present in the deposit after EBID are important for binding NH_3 . TDS data of NH_3 adsorbed on Fe deposit show that the main desorption peak already occurs around 120 K (see Fig. S12 in the supplementary material⁴⁶). Earlier TDS experiments with NH_3 adsorbed at temperatures around 35 K revealed the maximum of the multilayer desorption near 100 K^{57,65,66} which is the minimum attainable temperature of the bath cryostat used here. In the present experiments, the height of the NH_3 desorption peak did not increase significantly when the amount of NH_3 dosed onto the substrate was doubled (see Fig. S12 in the supplementary material⁴⁶). Therefore, the desorption signal is ascribed to a physisorbed monolayer. NH_3 that remains on the deposit surface at room temperature must, therefore, assume a chemisorbed state with specific binding to surface atoms of the deposit. This conclusion allows us to draw a closer comparison with the previous CVD studies.^{32,33}

The inhibition of AG on EBID deposits by NH_3 observed in the present study is reminiscent of the inhibition of CVD from $\text{Fe}(\text{CO})_5$ on oxide surfaces by the co-flow of NH_3 described previously,³³ despite the fact that CVD is a high-temperature process while AG on EBID layers proceeds at room temperature. As observed in Sec. III C, the oxygen content is larger in deposits grown by EBID from $\text{Fe}(\text{CO})_5$ than in those prepared by AG from the same precursor. Moreover, while the impure EBID deposits are structurally ill-defined and their surfaces likely to be dominated by defect sites, AG tends to yield materials with higher crystallinity.⁵ The binding strength of NH_3 on Fe(110) was determined as 0.74 eV.⁶⁷ Defects can increase the binding strength of an adsorbate significantly⁶⁸ and can, thus, contribute to the higher efficiency of the inhibition of AG from $\text{Fe}(\text{CO})_5$ on deposits prepared by EBID as compared to AG layers. In the case of the single crystal Fe(111) surface, the binding strength of NH_3 was also shown to increase when oxygen was preadsorbed.⁶⁹ Recent theoretical work has confirmed that the binding strength of NH_3 on Fe sites with adjacent O atoms in model systems consisting of different carbon-supported Fe oxides is significantly larger (up to around 2 eV)⁷⁰ than on

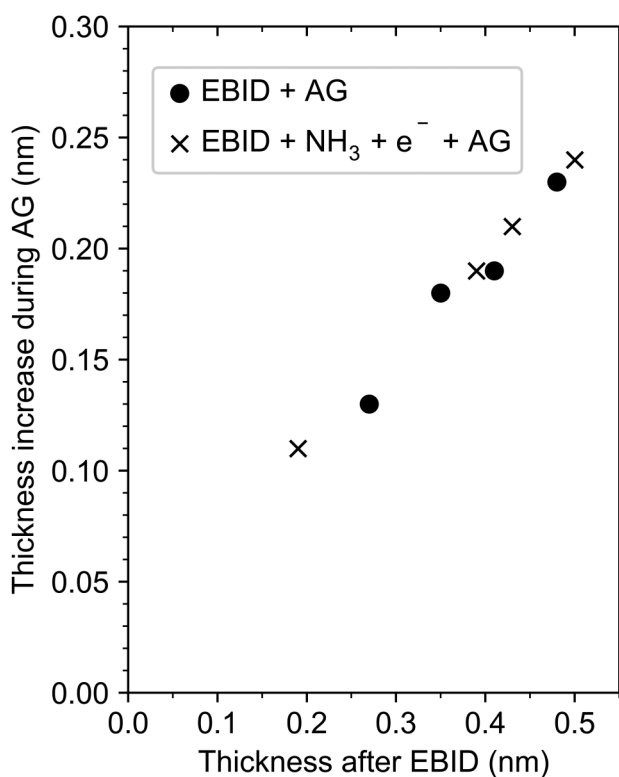


FIG. 9. Increase of the apparent deposit thickness during the AG steps of experiments 1–4 plotted as a function of the apparent thickness of the underlying EBID Fe layer. The apparent thickness of the deposit represents the value deduced from the attenuation of the Ta_{NNN} signals as described in Secs. II D and III A.

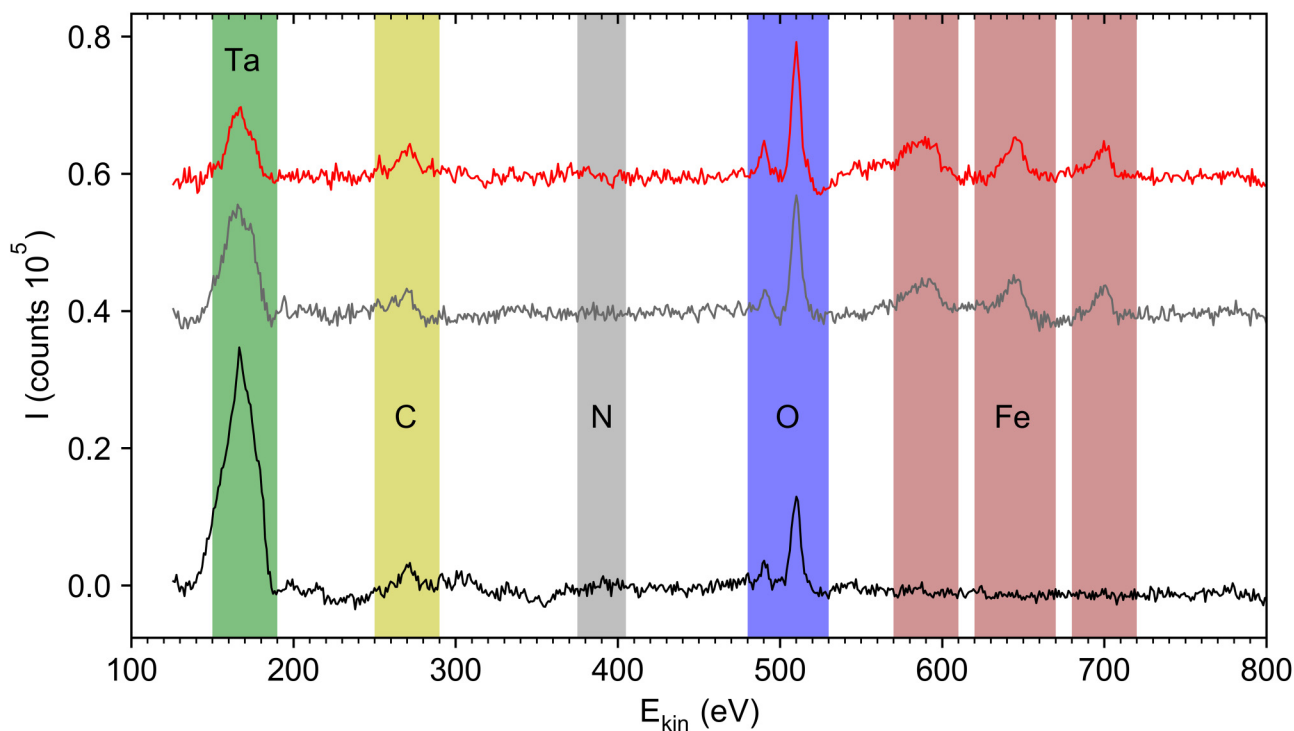


FIG. 10. Full range AES recorded on the freshly sputtered Ta substrate (black, bottom) and the same surface after simultaneous electron irradiation (500 eV) and dosing of $\text{Fe}(\text{CO})_5$ gas at room temperature followed by annealing to 450 K (EBID, dose corresponding to a pressure drop of 6 mTorr in the volume from which the gas is leaked, gray, middle), and after dosing of NH_3 (20 mTorr) at room temperature onto the EBID Fe layer and further electron irradiation (500 eV) (red, top). Note that the relatively high intensity of the O AES signal in this particular experiment relates to a larger partial pressure of residual H_2O in the UHV chamber leading to increased surface oxidation as compared to the previous experiments. For better visualization, a baseline correction has been applied to the three spectra. For clarity, the spectra are offset in the vertical direction.

nanoparticulate pure Fe (less than 0.4 eV),⁷¹ which we consider here as a model for the Fe seed deposits prepared by EBID. Overall, the lower binding strength on pure Fe as predicted by these studies rationalizes the lack of inhibition by NH_3 on an AG layer and indicates that impurities in the EBID layer are important for the inhibiting effect. We note, though, that NH_3 can dissociate on Fe surfaces already at room temperature.^{64,72} The theoretical studies predict that the barrier to dissociation yielding adsorbed NH_2 and H on nanoparticulate pure Fe is higher (near 1.5 eV)⁷¹ than on the carbon-supported Fe oxide models (down to around 0.7 eV).⁷⁰ We, therefore, cannot exclude that the inhibition of AG also relates to chemisorbed fragments of NH_3 , which are again converted to volatile N_2 by electron irradiation in the reactivation step.

The fact that decomposition of $\text{Fe}(\text{CO})_5$ is not inhibited on a deposit with higher Fe purity prepared by AG may relate to the findings of the previous CVD study that restored growth of Fe at 300 °C by the co-flow of NH_3 .³² However, the interpretation presented therein may have to be questioned. It was proposed that NH_3 blocks CO adsorption or displaces adsorbed CO from the growing Fe surface.³² However, a recent theoretical study predicted that binding of NH_3 on Fe(110) is considerably weaker than binding of CO on the same surface (0.62 eV for NH_3 and 1.91 eV

for CO).⁷³ Based on the reported dissociative adsorption of NH_3 on Fe already at room temperature,^{64,72} it appears possible that CO is removed from the surface via a reduction reaction instead of simple detachment. A more comprehensive theoretical study that accounts not only for a single crystal model surface but also for roughness as most likely encountered during surface deposition processes would be needed to gain more insight here.

IV. CONCLUSIONS

Thermal surface chemistry and, in particular, autocatalytic reactions can compromise the spatial control of deposit formation in focused electron beam induced deposition (FEBID) because they sustain deposition in the absence of electron irradiation. Aiming at an approach to control such thermal processes, we have performed surface science studies under UHV conditions. Fe seed deposits were prepared by dosing $\text{Fe}(\text{CO})_5$ onto a Ta substrate during electron irradiation. These deposits were used to investigate the effect of NH_3 on the subsequent autocatalytic growth (AG) of Fe from $\text{Fe}(\text{CO})_5$ as well as the anticipated reactivation of the surface by electron irradiation. The results of thermal desorption spectrometry (TDS) show that, at cryogenic temperature, $\text{Fe}(\text{CO})_5$ adsorbs

dissociatively on the Fe seed deposit, on layers prepared by AG, and on the underlying freshly sputter-cleaned Ta substrate. CO released upon dissociation begins to desorb below room temperature. This rationalizes the observation that AG can proceed at room temperature. However, Fe deposition by thermal surface reactions is considerably less efficient on the Ta substrate. We propose that this results from oxygen and carbon that remain bound to the surface as seen by Auger electron spectroscopy (AES) and impede further decomposition of Fe(CO)₅.

AES was, in particular, used to monitor the deposit growth and reveal the effect of NH₃ on the growth rate. The results indicate that Fe growth is not entirely inhibited, but AG is significantly slowed down when NH₃ is adsorbed on an Fe seed layer that contains contaminations of oxygen and carbon. This is in line with the previous finding that NH₃ can inhibit chemical vapor deposition (CVD) of Fe from Fe(CO)₅ on acidic oxide surfaces.³³ In contrast, our results show that this inhibition is not operative on layers with higher Fe content grown by a previous AG step. AG on the Fe seed layer can be restored by electron irradiation, which removes the adsorbed NH₃. More specifically, AES shows that this reactivation of the surface proceeds without nitride formation, suggesting that NH₃ is quantitatively converted to volatile species.

As a perspective for the development of improved FEBID processes, we propose that the co-flow of NH₃ can be beneficial to the spatial resolution of FEBID from Fe(CO)₅. Deposits prepared by FEBID are sufficiently contaminated to bind NH₃ at room temperature. When the beam scans elsewhere, the surface should thus be protected against AG by adsorbed NH₃. However, NH₃ is removed when the beam returns to a given site so that deposition from Fe(CO)₅ can continue. Co-injecting NH₃ during FEBID from Fe(CO)₅ is thus anticipated to be a viable strategy to suppress unwanted contributions of CVD to deposit growth.

AUTHOR DECLARATIONS

Conflict of Interest

The authors have no conflicts to disclose.

Author Contributions

Petra Martinović: Data curation (lead); Formal analysis (lead); Investigation (equal); Supervision (equal); Validation (lead); Visualization (lead); Writing – original draft (lead); Writing – review & editing (equal). **Lars Barnewitz:** Investigation (equal). **Markus Rohdenburg:** Software (lead). **Petra Swiderek:** Conceptualization (lead); Supervision (equal); Writing – review & editing (equal).

DATA AVAILABILITY

The data that support the findings of this study are available within the article and its supplementary material. The electronic raw data are available from the corresponding author upon reasonable request.

REFERENCES

¹H. Plank, R. Winkler, C. H. Schwalb, J. Hütner, J. D. Fowlkes, P. D. Rack, I. Utke, and M. Huth, *Micromachines* **11**, 48 (2020).

- ²I. Utke, P. Hoffmann, and J. Melngailis, *J. Vac. Sci. Technol. B* **26**, 1197 (2008).
³R. M. Thorman, R. Kumar T P, D. H. Fairbrother, and O. Ingólfsson, *Beilstein J. Nanotechnol.* **6**, 1904 (2015).
⁴O. Ingólfsson, *Low-energy Electrons, Fundamentals and Applications* (Pan Stanford Publishing, Singapore, 2019). Vol. 1.
⁵I. Utke, P. Swiderek, K. Höflich, K. Madajska, J. Jurczyk, P. Martinović, and I. B. Szymańska, *Coord. Chem. Rev.* **458**, 213851 (2022).
⁶A. Botman, J. J. L. Mulders, and C. W. Hagen, *Nanotechnology* **20**, 372001 (2009).
⁷B. Geier *et al.*, *J. Phys. Chem. C* **118**, 14009 (2014).
⁸D. Belić, M. M. Shawrav, M. Gavagnin, M. Stöger-Pollach, H. D. Wanzenboeck, and E. Bertagnolli, *ACS Appl. Mater. Interfaces* **7**, 2467 (2015).
⁹M. Rohdenburg, R. Winkler, D. Kuhness, H. Plank, and P. Swiderek, *ACS Appl. Nano Mater.* **3**, 8352 (2020).
¹⁰I. Utke, A. Luisier, P. Hoffmann, D. Laub, and P. A. Buffat, *Appl. Phys. Lett.* **81**, 3245 (2002).
¹¹K. Höflich, J. Jurczyk, Y. Zhang, M. V. Puydinger Dos Santos, M. Götz, C. Guerra-Núñez, J. P. Best, C. Kapusta, and I. Utke, *ACS Appl. Mater. Interfaces* **9**, 24071 (2017).
¹²G. Hochleitner, H. D. Wanzenboeck, and E. Bertagnolli, *J. Vac. Sci. Technol. B* **26**, 939 (2008).
¹³F. Vollnhals, P. Wintrich, M.-M. Walz, H.-P. Steinrück, and H. Marbach, *Langmuir* **29**, 12290 (2013).
¹⁴T. Lukaszczuk, M. Schirmer, H.-P. Steinrück, and H. Marbach, *Langmuir* **25**, 11930 (2009).
¹⁵F. Tu, M. Drost, F. Vollnhals, A. Späth, E. Carrasco, R. H. Fink, and H. Marbach, *Nanotechnology* **27**, 355302 (2016).
¹⁶H. Marbach, *Appl. Phys. A* **117**, 987 (2014).
¹⁷M. Drost, F. Tu, F. Vollnhals, I. Szent, J. Kiss, and H. Marbach, *Small Methods* **1**, 1700095 (2017).
¹⁸M. Drost, F. Tu, L. Berger, C. Preischl, W. Zhou, H. Gliemann, C. Wöll, and H. Marbach, *ACS Nano* **12**, 3825 (2018).
¹⁹T. Lukaszczuk, M. Schirmer, H.-P. Steinrück, and H. Marbach, *Small* **4**, 841 (2008).
²⁰F. Zaera, *Surf. Sci.* **255**, 280 (1991).
²¹F. Zaera, *Coord. Chem. Rev.* **257**, 3177 (2013).
²²F. Zaera, *Langmuir* **7**, 1188 (1991).
²³J. R. Swanson, C. M. Friend, and Y. J. Chabal, *J. Chem. Phys.* **87**, 5028 (1987).
²⁴M. A. Henderson, R. D. Ramsier, and J. T. Yates, *Surf. Sci.* **259**, 173 (1991).
²⁵M. N. Rocklein and D. P. Land, *Surf. Sci.* **436**, L702 (1999).
²⁶S. Sato and S. Tanaka, *Appl. Surf. Sci.* **135**, 83 (1998).
²⁷L. Sun and E. M. McCash, *Surf. Sci.* **422**, 77 (1999).
²⁸T. Tanabe, T. Morisato, Y. Suzuki, Y. Matsumoto, T. Wadayama, and A. Hatta, *Vib. Spectrosc.* **18**, 141 (1998).
²⁹T. Tanabe, K. Kubo, T. Ishibashi, T. Wadayama, and A. Hatta, *Appl. Surf. Sci.* **207**, 115 (2003).
³⁰J. Oh, T. Kondo, D. Hatake, K. Arakawa, T. Suzuki, D. Sekiba, and J. Nakamura, *J. Phys. Chem. C* **116**, 7741 (2012).
³¹H. H. Huang, C. S. Sreekanth, C. S. Seet, G. Q. Xu, and L. Chan, *J. Phys. Chem.* **100**, 18138 (1996).
³²P. Zhang, E. Mohimi, T. K. Talukdar, J. R. Abelson, and G. S. Girolami, *J. Vac. Sci. Technol. A* **34**, 051518 (2016).
³³E. Mohimi, Z. V. Zhang, S. Liu, J. L. Mallek, G. S. Girolami, and J. R. Abelson, *J. Vac. Sci. Technol. A* **36**, 041507 (2018).
³⁴R. R. Kunz, *J. Vac. Sci. Technol. B* **6**, 1557 (1988).
³⁵M. Xu and F. Zaera, *J. Vac. Sci. Technol. A* **14**, 415 (1996).
³⁶M.-M. Walz, M. Schirmer, F. Vollnhals, T. Lukaszczuk, H.-P. Steinrück, and H. Marbach, *Angew. Chem. Int. Ed.* **49**, 4669 (2010).
³⁷M.-M. Walz, F. Vollnhals, F. Rietzler, M. Schirmer, A. Kunzmann, H.-P. Steinrück, and H. Marbach, *J. Phys. D: Appl. Phys.* **45**, 225306 (2012).
³⁸Z. V. Zhang, S. Liu, G. S. Girolami, and J. R. Abelson, *J. Vac. Sci. Technol. A* **38**, 033401 (2020).

- ³⁹M. Rohdenburg, P. Martinović, K. Ahlenhoff, S. Koch, D. Emmrich, A. Gölzhäuser, and P. Swiderek, *J. Phys. Chem. C* **123**, 21774 (2019).
- ⁴⁰M. Rohdenburg, H. Boeckers, C. R. Brewer, L. McElwee-White, and P. Swiderek, *Sci. Rep.* **10**, 10901 (2020).
- ⁴¹J. Warneke, M. Rohdenburg, Y. Zhang, J. Orszagh, A. Vaz, I. Utke, J. T. M. de Hosson, W. F. van Dorp, and P. Swiderek, *J. Phys. Chem. C* **120**, 4112 (2016).
- ⁴²Z. Warneke, M. Rohdenburg, J. Warneke, J. Kopyra, and P. Swiderek, *Beilstein J. Nanotechnol.* **9**, 77 (2018).
- ⁴³I. Ipolyi, W. Michaelis, and P. Swiderek, *Phys. Chem. Chem. Phys.* **9**, 180 (2007).
- ⁴⁴S. G. Rosenberg, M. Barclay, and D. H. Fairbrother, *J. Phys. Chem. C* **117**, 16053 (2013).
- ⁴⁵J. A. Spencer, J. A. Brannaka, M. Barclay, L. McElwee-White, and D. H. Fairbrother, *J. Phys. Chem. C* **119**, 15349 (2015).
- ⁴⁶See supplementary material at <https://www.scitation.org/doi/suppl/10.1116/6.0002306> for additional spectra and experimental data.
- ⁴⁷P. J. Cumpson and M. P. Seah, *Surf. Interface Anal.* **25**, 430 (1997).
- ⁴⁸D. Briggs, *Surface Analysis by Auger and X-ray Photoelectron Spectroscopy* (IM, Chichester, 2003).
- ⁴⁹E. Bilgiliyos, J.-C. Yu, C. Preischl, L. McElwee-White, H.-P. Steinrück, and H. Marbach, *ACS Appl. Nano Mater.* **5**, 3855 (2022).
- ⁵⁰B. Götz, O. Kröhl, and P. Swiderek, *J. Electron Spectros. Relat. Phenom.* **114–116**, 569 (2001).
- ⁵¹N. Nakayama, H. Tanabe, A. Satoh, Y. Mugita, A. Nakatsuka, S. Nagata, and Y. Ueda, *Trans. Mater. Res. Soc.* **33**, 893 (2008).
- ⁵²S. Sato, Y. Ukisu, H. Ogawa, and Y. Takasu, *J. Chem. Soc., Faraday Trans.* **89**, 4387 (1993).
- ⁵³S. Sato and T. Suzuki, *J. Phys. Chem.* **100**, 14769 (1996).
- ⁵⁴I. Ipolyi and P. Swiderek, *Surf. Sci.* **602**, 3199 (2008).
- ⁵⁵P. Jakob and D. Menzel, *Surf. Sci.* **220**, 70 (1989).
- ⁵⁶P. Swiderek and H. Winterling, *Chem. Phys.* **229**, 295 (1998).
- ⁵⁷E. Böhler, J. H. Bredehöft, and P. Swiderek, *J. Phys. Chem. C* **118**, 6922 (2014).
- ⁵⁸J. H. Campbell, C. Bäter, W. G. Durrer, and J. H. Craig, *Thin Solid Films* **295**, 8 (1997).
- ⁵⁹F. Schmidt, T. Borrmann, M. P. Mues, S. Benter, P. Swiderek, and J. H. Bredehöft, *Atoms* **10**, 25 (2022).
- ⁶⁰Y.-M. Sun, D. Sloan, H. Ihm, and J. M. White, *J. Vac. Sci. Technol. A* **14**, 1516 (1996).
- ⁶¹S. C. Yeo, Y. C. Lo, J. Li, and H. M. Lee, *J. Chem. Phys.* **141**, 134108 (2014).
- ⁶²W. Arabczyk and R. Pelka, *J. Phys. Chem. A* **113**, 411 (2009).
- ⁶³R. Pelka, K. Kielbasa, and W. Arabczyk, *J. Phys. Chem. C* **118**, 6178 (2014).
- ⁶⁴G. Ertl, M. Huber, and N. Thiele, *Z. Naturforsch. A* **34**, 30 (1979).
- ⁶⁵T. Hamann, E. Böhler, and P. Swiderek, *Angew. Chem. Int. Ed.* **48**, 4643 (2009).
- ⁶⁶J. H. Bredehöft, E. Böhler, F. Schmidt, T. Borrmann, and P. Swiderek, *ACS Earth Space Chem.* **1**, 50 (2017).
- ⁶⁷M. Weiss, G. Ertl, and F. Nitschké, *Appl. Surf. Sci.* **2**, 614 (1979).
- ⁶⁸S. Wang, Y.-M. Sun, Q. Wang, and J. M. White, *J. Vac. Sci. Technol. B* **22**, 1803 (2004).
- ⁶⁹P. Iyngaran, D. C. Madden, D. A. King, and S. J. Jenkins, *J. Phys. Chem. C* **121**, 24594 (2017).
- ⁷⁰C. Xie, Y. Sun, B. Zhu, W. Song, and M. Xu, *New J. Chem.* **45**, 3169 (2021).
- ⁷¹G. Lanzani and K. Laasonen, *Int. J. Hydrog. Energy* **35**, 6571 (2010).
- ⁷²K. Yoshida and G. A. Somorjai, *Surf. Sci.* **75**, 46 (1978).
- ⁷³L. Xu, D. Kirvassilis, Y. Bai, and M. Mavrikakis, *Surf. Sci.* **667**, 54 (2018).